

Topological waves in photonic mesh lattices based on coupled optical fiber loops (Semester Project)

Haiwei Wang
Section of Microengineering

EPFL, Lausanne
January 25, 2025
Laboratory of Wave Engineering

Professor: Romain Fleury

Supervisor: Zhe Zhang, Junda Wang, Ji Zhou

Abstract

The coupled optical fiber loops as a platform for synthetic topological lattices and quantum walk is studied. By time multiplexing, it can create robust, large-scale lattices with high flexibility to introduce spatial and temporal modulation. For theoretical part of this report, the Floquet SSH lattice is the main focus. The band structure and topological invariants are calculated by firstly mapping the discrete lattice to a continuous-time time-dependent Hamiltonian. And the boundary states at the interface of two bulk lattices with different topological phases are observed in simulation, which shows a unique characteristic related to the Floquet system. Finally, a simple experimental setup is built which can achieve a few steps of propagation in a basic photonic mesh lattice. Further work should focus on improving the performance and functionality of the setup.

Contents

Abstract	2
1 Introduction	4
2 Theory	4
2.1 From coupled optical fiber loops to photonic mesh lattices	4
2.2 Band structure of different lattices	5
2.2.1 Band structure of a simple basic lattice	5
2.2.2 Band structure of a lattice with on-site potential	7
2.2.3 The Floquet SSH lattice	8
2.3 Gap topological invariants of SSH lattice	11
3 Simulation	18
3.1 Code overview	18
3.2 Evolution in a simple basic lattice	18
3.3 Evolution in the SSH lattice	19
3.4 Evolution in a nonlinear lattice	20
4 Experiment	20
4.1 Typical setup in papers	20
4.2 Current setup	22
4.3 Future work	25
5 Conclusion	26
6 Acknowledgements	26
References	27
Appendix A: Influence of phase ambiguity in the coupler and loops	29
Appendix B: Quantum walk formulation of the Floquet SSH lattice	31
Appendix C: Extending the experimentally reachable region in the phase diagram	34

1 Introduction

This report summarizes my investigation on the coupled optical fiber loops for synthetic photonic mesh lattices. The topological phase in this structure is the main focus. This setup features a large-scale lattice and high flexibility of modulation in the field of topological photonics. It is based on conventional optical communication components and does not need careful optical alignment. Since its invention as a platform to study the interplay of coherence and losses[1], the setup has been widely used for optical non-Hermitian system[2–7]. It has also been used to study nonlinear effects in topological photonics[8] and most recently, time interfaces in a lattice[9, 10].

The report will be structured as follows: First, the principle of time multiplexing in the coupled optical fiber loops is introduced, which essentially creates a photonic mesh lattice with one spatial and one temporal dimension. The band structure of some typical lattices is calculated. Among them the Floquet SSH lattice, which is similar to the famous Su–Schrieffer–Heeger (SSH) model in topological insulator, is our main focus. Due to its Floquet nature, the topological invariant related to a bandgap is calculated, instead of the one related to a band. Then, the evolution of optical pulses in the lattices is simulated, showing the boundary states between two lattices with different topological phases. Finally, an experimental setup is built with minimum components and a few steps of propagation is successfully observed. However, further work needs to be done to improve the experimental setup and construct the topological interface.

2 Theory

2.1 From coupled optical fiber loops to photonic mesh lattices

The coupled optical fiber loops consist of two loops with different length joint by a coupler, as shown in Fig 2.1(b). A pulse circulating in it will be split into two at the coupler, and the two subsequent pulses will arrive at the coupler at different time, which will be further split into the long and short loop. Only the pulses that arrive at the coupler at the same time can interfere, which corresponds to pulses that go through the same times in the long and short loop (equal roundtrips in the long loop, and equal roundtrips in the short loop, see Fig 2.1(a)). So it can be mapped to a mesh lattice as shown in Fig 2.1(c).

The advantage of using coupled optical fiber loops and time multiplexing is that it offers

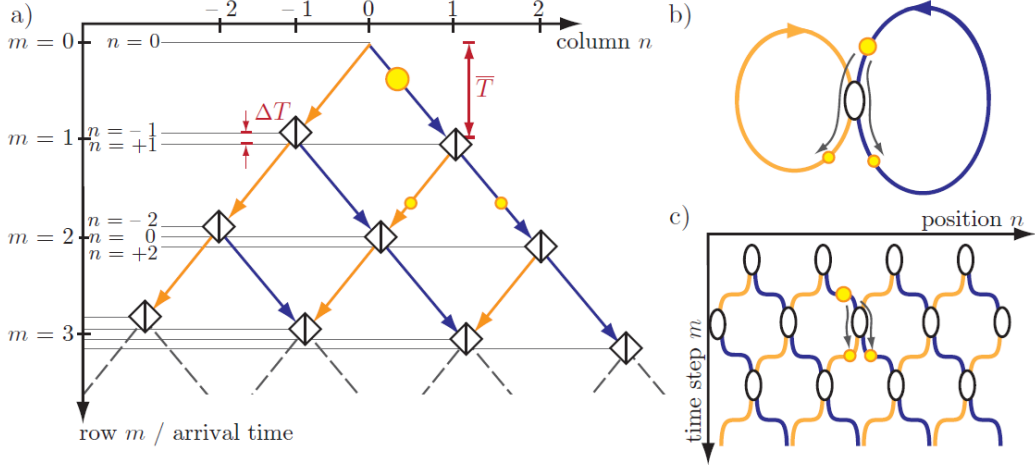


Figure 2.1: The principle of time multiplexing to create a photonic mesh lattice (From Ref [11]). A roundtrip in the short (long) loop in (b) corresponds to the motion to the left (right) in the pyramid (a). It can also be represented by a 2D lattice as shown in (c).

great scalability. For quantum walk experiments using real space as the lattice sites, the number of walking is limited to ~ 10 steps[12]. However, for a coupled optical fiber loops setup, more than 100 steps is routinely reported. The interference of pulses does not rely on careful optical alignment, instead it is guaranteed by the same arrival time at the coupler because the pulses have the same roundtrips in each loop. Moreover, when using intensity and phase modulators and variable coupler, we can create complex lattices with varying parameters in both dimensions, enabling its applications in Floquet system, non-Hermitian system, and topological boundary.

2.2 Band structure of different lattices

2.2.1 Band structure of a simple basic lattice

For a basic mesh lattice with 50/50 coupler and without any phase modulation, gain/loss, or nonlinearity, as shown in Fig 2.2(a), the single step propagation ($m+1$) can be written as

$$a_{n+1}^{m+1} = \frac{1}{\sqrt{2}}(a_n^m + i b_n^m)$$

$$b_{n+1}^{m+1} = \frac{1}{\sqrt{2}}(i a_{n+2}^m + b_{n+2}^m)$$

Here, a and b represents the complex amplitude of the pulse in the long loop and short loop, respectively. The index m is the propagation step, and the index n is the temporal position within one roundtrip of the pulses.

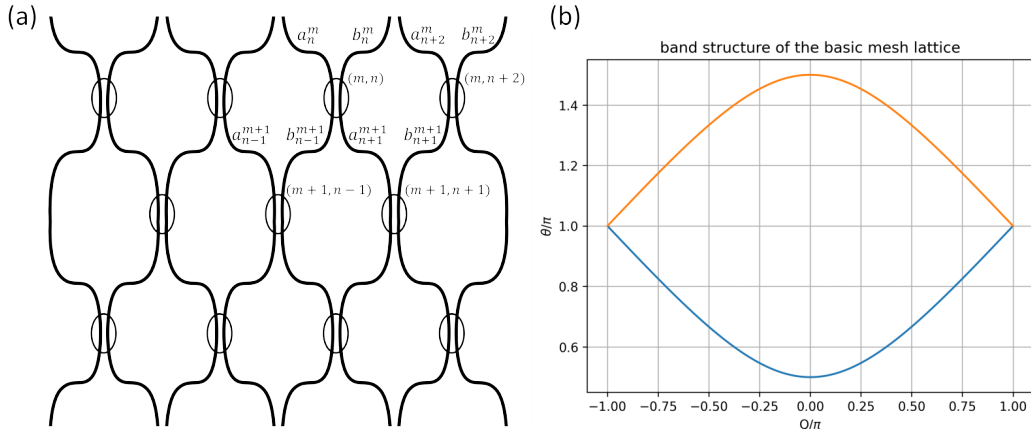


Figure 2.2: A simple basic mesh lattice with 50/50 couplers. A sketch of the lattice is shown in (a). The band structure is shown in (b).

One thing that should not be confused is that in reality, the light pulse will acquire a $\pi/2$ phase shift when crossing the coupler (in contrast to passing the coupler), going from one loop to another, which is, however, shown as passing the coupler in the sketch.

Due to the periodicity of the lattice, we can assume a plane wave ansatz and obtain the dispersion relation (band structure).

$$\begin{pmatrix} a_n^{m+2} \\ b_n^{m+2} \end{pmatrix} = \begin{pmatrix} a_n^m \\ b_n^m \end{pmatrix} e^{i\theta}$$

$$\begin{pmatrix} a_{n+2}^m \\ b_{n+2}^m \end{pmatrix} = \begin{pmatrix} a_n^m \\ b_n^m \end{pmatrix} e^{iQ}$$

we can get

$$2 \cos(\theta) = \cos(Q) - 1$$

so

$$\theta = \pm \cos^{-1}\left(\frac{\cos(Q) - 1}{2}\right)$$

This is shown in Fig 2.2(b). A more detailed and introductory discussion can be found in Ref [2].

2.2.2 Band structure of a lattice with on-site potential

Now we add a phase modulation to each pulse in the long loop by following the scheme in Ref [3].

$$\varphi(n) = \begin{cases} -\varphi_0 & \text{for } \text{mod}(n+3;4) = 0;1 \\ +\varphi_0 & \text{for } \text{mod}(n+3;4) = 2;3. \end{cases}$$

When exciting the lattice with a single pulse at the position of $n = 0$, the pulses in every roundtrip will only occupy either even or odd positions of n . By applying this phase modulation, we can get alternative phase modulation for the pulses within one roundtrip, as shown in Fig 2.3(a).

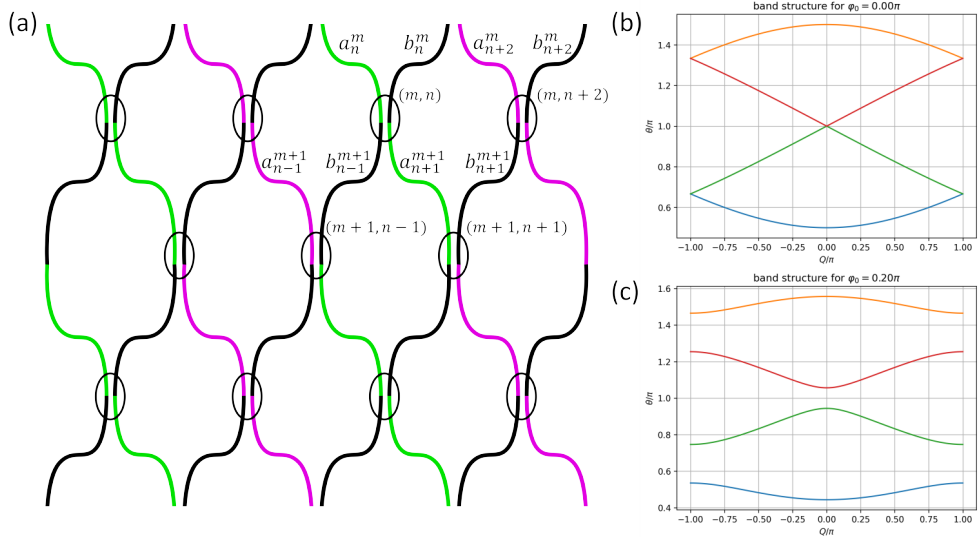


Figure 2.3: A mesh lattice with phase modulation. A sketch of the lattice is shown in (a). The green and magenta lines represent $-\varphi_0$ and $+\varphi_0$ modulation, respectively. The band structure of different phase modulation is shown in (b) and (c).

Now the evolution can be written as

$$\begin{aligned} a_{n+1}^{m+1} &= \frac{1}{\sqrt{2}}(a_n^m + i b_n^m) e^{i\varphi(n+1)} \\ b_{n+1}^{m+1} &= \frac{1}{\sqrt{2}}(i a_{n+2}^m + b_{n+2}^m) \end{aligned}$$

The plane wave ansatz now becomes

$$\begin{pmatrix} a_n^{m+2} \\ b_n^{m+2} \end{pmatrix} = \begin{pmatrix} a_n^m \\ b_n^m \end{pmatrix} e^{i\theta}$$

$$\begin{pmatrix} a_{n+4}^m \\ b_{n+4}^m \end{pmatrix} = \begin{pmatrix} a_n^m \\ b_n^m \end{pmatrix} e^{iQ}$$

From above we can again solve for the dispersion relation (band structure)

$$\cos(Q) = 8\cos^2(\theta) + 8\cos(\varphi_0)\cos(\theta) + 4\cos^2(\varphi_0) - 3$$

To get this equation, one can first get 4 equations for $a_0^0, b_0^0, a_2^0, b_2^0$ and write in matrix form $AX = 0$, where X is the 4 dimensional vector containing $a_0^0, b_0^0, a_2^0, b_2^0$ and A is the 4x4 matrix containing θ, Q , and φ_0 . Then one can solve for the relation between θ and Q by setting the determinant of A to be 0. The calculation can be done by using the symbolic toolbox in MATLAB or by similar software.

2.2.3 The Floquet SSH lattice

The Floquet SSH lattice is governed by the following equations:

$$\begin{aligned} a_{n+1}^{m+1} &= \cos(\beta^m) a_n^m + i \sin(\beta^m) b_n^m \\ b_{n+1}^{m+1} &= i \sin(\beta^m) a_{n+2}^m + \cos(\beta^m) b_{n+2}^m \end{aligned}$$

where

$$\beta^m = \begin{cases} \beta_o, & m = 1, 3, 5, \dots \\ \beta_e, & m = 2, 4, 6, \dots \end{cases}$$

which represents a lattice with two splitting ratio switch from step to step, as shown in Fig 2.4. The reason why it is called Floquet SSH will be clear in the next section.

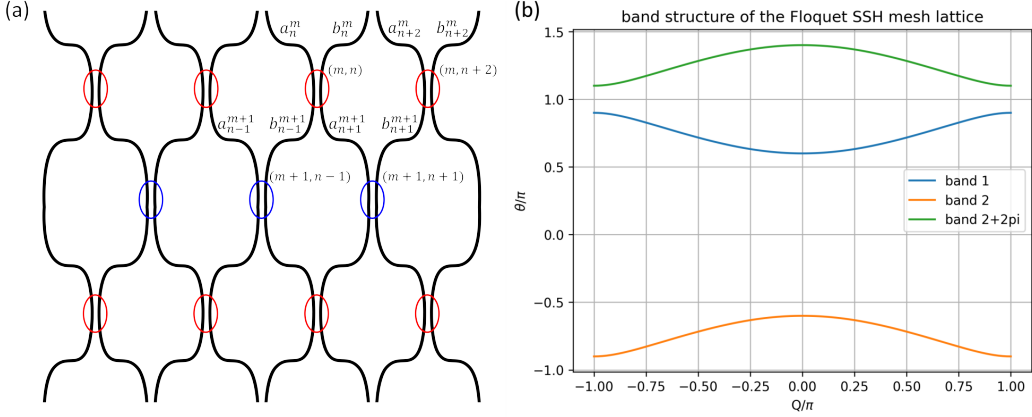


Figure 2.4: The Floquet SHH lattice. A sketch of the lattice is shown in (a). The red and blue couplers have β_o and β_e respectively. The band structure for $\beta_o = 0.25\pi$, $\beta_e = 0.35\pi$ is shown in (b). The 0 gap and π gap are shown. All quasienergy θ is periodic in 2π due to the Floquet nature.

The translational symmetry gives

$$\begin{pmatrix} a_n^{m+2} \\ b_n^{m+2} \end{pmatrix} = \begin{pmatrix} a_n^m \\ b_n^m \end{pmatrix} e^{i\theta}$$

$$\begin{pmatrix} a_{n+2}^m \\ b_{n+2}^m \end{pmatrix} = \begin{pmatrix} a_n^m \\ b_n^m \end{pmatrix} e^{iQ}$$

Use the equations above we can get:

$$\begin{pmatrix} A & B \\ C & D \end{pmatrix} \begin{pmatrix} a_n^m \\ b_n^m \end{pmatrix} = 0$$

where A, B, C, D are expressions containing $Q, \theta, \beta_o, \beta_e$.

$$\begin{aligned} A &= \cos(\beta_e) \cos(\beta_o) e^{-iQ} - \sin(\beta_e) \sin(\beta_o) - e^{i\theta} \\ B &= i \cos(\beta_e) \sin(\beta_o) e^{-iQ} + i \sin(\beta_e) \cos(\beta_o) \\ C &= i \cos(\beta_e) \sin(\beta_o) e^{iQ} + i \sin(\beta_e) \cos(\beta_o) \\ D &= \cos(\beta_e) \cos(\beta_o) e^{iQ} - \sin(\beta_e) \sin(\beta_o) - e^{i\theta} \end{aligned}$$

To have non-zero solutions of a_n^m, b_n^m , we need the determinant of the ABCD matrix to be zero. We get

$$\cos(\theta) = \cos(\beta_o) \cos(\beta_e) \cos(Q) - \sin(\beta_o) \sin(\beta_e)$$

so

$$\theta = \pm \cos^{-1}(\cos(\beta_o) \cos(\beta_e) \cos(Q) - \sin(\beta_o) \sin(\beta_e))$$

We then solve for the Bloch state a, b to satisfy

$$\begin{pmatrix} A & B \\ C & D \end{pmatrix} \begin{pmatrix} a_n^m \\ b_n^m \end{pmatrix} = 0$$

for two θ at each Q .

$$\begin{aligned} \vec{X}_1 &= \frac{1}{\sqrt{1 + \left| \frac{A_1}{B} \right|^2}} \begin{pmatrix} 1 \\ -\frac{A_1}{B} \end{pmatrix} \\ \vec{X}_2 &= \frac{1}{\sqrt{1 + \left| \frac{A_2}{B} \right|^2}} \begin{pmatrix} 1 \\ -\frac{A_2}{B} \end{pmatrix} \end{aligned}$$

The Berry's phase (Zak phase) for each band is defined as

$$\gamma = i \int_0^{2\pi} \langle X | \partial_Q | X \rangle dQ$$

The integral can be solved numerically for given β_o, β_e . In Appendix B an alternative derivation of the dispersion relation and the band invariants is provided, which is based on the quantum walk formulation.

2.3 Gap topological invariants of SSH lattice

The Berry's phase defined above is one way to get the band topological invariants of a topological insulator. However, this is not the true invariants for the Floquet SSH lattice, as it fails to predict the number of boundary states between two bulk lattices. Here, we follow the recipe given in Ref [13] to calculate the topological invariants assigned to the bandgap, rather than to the band. To begin with, one first needs to map our discrete-time lattice to a continuous-time Hamiltonian, for which we can apply all the tools given in Ref [13].

As shown in the Fig 2.5, the Floquet SSH lattice can be directly mapped to a periodically-driven 1D chain. Here the site index in the mesh lattice is no longer defined by the position of the coupler, but by pulses themselves in the two loops. The alternating coupling coefficient in the canonical SSH model is switch on and off in turn, corresponding to a periodic modulation of the coupling. The good thing is that the coupling strength can be related to the splitting parameter β in the couplers.

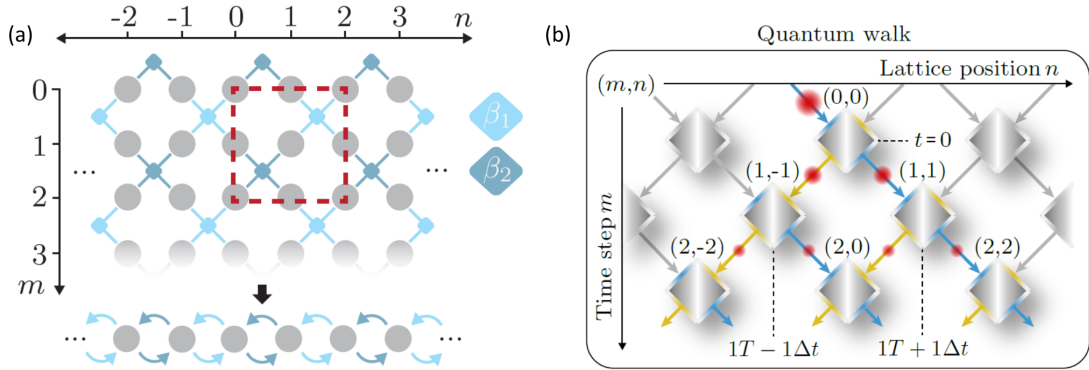


Figure 2.5: The map from the mesh lattice (b) to a one dimensional chain with time-modulated coupling (a), which is known as the Floquet SSH model. Note the different way of numbering in (a) and (b). From Ref [14].

We define the period to be $T = 1$, corresponding to two steps of evolution in the mesh lattice or two roundtrips in the coupled fiber loops. And each step of evolution takes time $T/2$.

The Bloch Hamiltonian for the 1D lattice is

$$H(k, t) = \begin{pmatrix} 0 & v(t) + w(t)e^{-ik} \\ v(t) + w(t)e^{ik} & 0 \end{pmatrix}$$

where

$$v(t) = \begin{cases} v, & 0 \leq t < \frac{T}{2} \\ 0, & \frac{T}{2} \leq t < T \end{cases}; w(t) = \begin{cases} 0, & 0 \leq t < \frac{T}{2} \\ w, & \frac{T}{2} \leq t < T \end{cases}$$

and $v(t+T) = v(t)$, $w(t+T) = w(t)$, $H(k, t+T) = H(k, t)$.

Now let's find the relation between v, w and β_o, β_e .

The evolution of one step within a unit cell gives

$$\begin{pmatrix} a(k, T/2) \\ b(k, T/2) \end{pmatrix} = \begin{pmatrix} i \sin(\beta) & \cos(\beta) \\ \cos(\beta) & i \sin(\beta) \end{pmatrix} \begin{pmatrix} a(k, 0) \\ b(k, 0) \end{pmatrix}$$

Notice that here the a, b swap between the long and short loops after passing through the coupler.

The evolution during the first half of the period can be solved as

$$\begin{aligned} a(k, \frac{T}{2}) &= \cos\left(v \frac{T}{2}\right) a(k, 0) - i \sin\left(v \frac{T}{2}\right) b(k, 0) \\ b(k, \frac{T}{2}) &= \cos\left(v \frac{T}{2}\right) b(k, 0) - i \sin\left(v \frac{T}{2}\right) a(k, 0) \end{aligned}$$

We can find that $v \frac{T}{2} = \frac{\pi}{2} - \beta$ makes the two set of equations equivalent, up to a global phase factor which does nothing to the physical observables. Since we have defined $T = 1$ and the first setup to be β_o , we get

$$v = \pi - 2\beta_o$$

Similarly, the evolution during the second half of the period can be solved as

$$\begin{aligned} a(k, \frac{T}{2}) &= \cos\left(w \frac{T}{2}\right) a(k, 0) - i e^{-ik} \sin\left(w \frac{T}{2}\right) b(k, 0) \\ b(k, \frac{T}{2}) &= \cos\left(w \frac{T}{2}\right) b(k, 0) - i e^{ik} \sin\left(w \frac{T}{2}\right) a(k, 0) \end{aligned}$$

This looks like impossible to map back to the mesh lattice coupler. But we have to remember that this is the coupling between two different unit cells and hence the e^{ik} factor is natural

from the Bloch theorem.

$$\begin{pmatrix} a(k, T/2) \\ b(k, T/2) \end{pmatrix} = \begin{pmatrix} i \sin(\beta) & e^{-ik} \cos(\beta) \\ e^{ik} \cos(\beta) & i \sin(\beta) \end{pmatrix} \begin{pmatrix} a(k, 0) \\ b(k, 0) \end{pmatrix}$$

We can similarly get

$$w = \pi - 2\beta_e$$

By far, we have successfully mapped the discrete-time mesh lattice to a continuous-time Floquet SSH lattice. We shift the time origin of the Hamiltonian by $T/4$ to make it symmetric:

$$H(k, t) = \begin{pmatrix} 0 & v(t) + w(t)e^{-ik} \\ v(t) + w(t)e^{ik} & 0 \end{pmatrix}$$

where

$$v(t) = \begin{cases} v, & 0 \leq t < \frac{T}{4} \\ 0, & \frac{T}{4} \leq t < \frac{T}{2} \\ 0, & \frac{T}{2} \leq t < \frac{3T}{4} \\ v, & \frac{3T}{4} \leq t < T \end{cases}; \quad w(t) = \begin{cases} 0, & 0 \leq t < \frac{T}{4} \\ w, & \frac{T}{4} \leq t < \frac{T}{2} \\ w, & \frac{T}{2} \leq t < \frac{3T}{4} \\ 0, & \frac{3T}{4} \leq t < T \end{cases}$$

Remember that $T = 1$, $v = \pi - 2\beta_o$ and $w = \pi - 2\beta_e$.

As a general rule, the action of a time-independent Hamiltonian on a 2 level system is rotating the Bloch vector around an axis. A rotation in the Bloch sphere is characterized by

$$R_n(\alpha) = e^{-i\frac{\alpha}{2}\vec{n}\cdot\vec{\sigma}} = \cos\left(\frac{\alpha}{2}\right)I - i \sin\left(\frac{\alpha}{2}\right)\vec{n}\cdot\vec{\sigma}$$

where \vec{n} is the axis and α is the angle of rotation (use right-hand rule).

The Hamiltonian $H(k, t)$ can be decomposed with the Pauli matrices. During the time when v is activated, we have

$$H(k, t) = \begin{pmatrix} 0 & v \\ v & 0 \end{pmatrix} = v\sigma_x$$

and during the time when w is activated, we have

$$H(k, t) = \begin{pmatrix} 0 & we^{-ik} \\ we^{ik} & 0 \end{pmatrix} = w \cos(k)\sigma_x + w \sin(k)\sigma_y$$

and for a time-independent Hamiltonian, the evolution operator is

$$U(t) = e^{-iHt}$$

Let's start to construct the topological invariants from the Bloch Hamiltonian $H(k, t)$. The time evolution operator is

$$U(k, t) = \mathcal{T} e^{-i \int_0^t H(k, t') dt'}$$

For our case, the $H(k, t)$ is piece-wise constant, so the integration can be easily calculated just by dividing the time into intervals. The full-period time evolution operator is

$$\begin{aligned} U(k, t=1) &= e^{-i\frac{1}{4}\nu\sigma_x} e^{-i\frac{1}{2}(w\cos(k)\sigma_x + w\sin(k)\sigma_y)} e^{-i\frac{1}{4}\nu\sigma_x} \\ &= \left[\cos\left(\frac{\nu}{2}\right) \cos\left(\frac{w}{2}\right) - \sin\left(\frac{\nu}{2}\right) \sin\left(\frac{w}{2}\right) \cos(k) \right] I \\ &\quad - i \left[\sin\left(\frac{\nu}{2}\right) \cos\left(\frac{w}{2}\right) + \cos\left(\frac{\nu}{2}\right) \sin\left(\frac{w}{2}\right) \cos(k) \right] \sigma_x \\ &\quad - i \sin\left(\frac{w}{2}\right) \sin(k) \sigma_y \\ &= \lambda_1(k) |\psi_1(k)\rangle\langle\psi_1(k)| + \lambda_2(k) |\psi_2(k)\rangle\langle\psi_2(k)| \end{aligned}$$

We can find the eigenvalue of $U(k, t=1)$ by noticing that $U(k, t=1) = a_0 I - i(a_x\sigma_x + a_y\sigma_y)$. Therefore, the eigenvectors of $U(k, t=1)$ is also the eigenvectors of $a_x\sigma_x + a_y\sigma_y$, which has eigenvalues $\pm\sqrt{a_x^2 + a_y^2}$. Therefore, the eigenvalues of $U(k, t=1)$ are

$$\lambda_{1,2}(k) = a_0 \mp i\sqrt{a_x^2 + a_y^2}$$

with eigenvectors

$$|\psi_{1,2}(k)\rangle = \frac{1}{\sqrt{2}} \begin{pmatrix} \pm \frac{i\sqrt{a_x^2 + a_y^2}}{-a_y + ia_x} \\ 1 \end{pmatrix}$$

The band structure can be obtained by solving the equation $\lambda_{1,2}(k) = e^{-iE}$. Later we will show that the chiral symmetry of the Hamiltonian results in the closing of the gap at $E = q\pi$ for integer q . In the interval of $-\pi \leq E \leq \pi$, if the band gap closes at $E = 0$, we have $\lambda_{1,2}(k) = 1$, which gives

$$\begin{aligned} a_0 &= 1 \\ a_x^2 + a_y^2 &= 0 \end{aligned}$$

$a_0 = 1$ requires $\cos(k) = \pm 1$, which means $k = q'\pi$ where q' is an integer, and at the same time makes $a_y = 0$. We can find that the bandgap closes at $E = 0, k = 0$ when $\frac{\nu}{2} + \frac{w}{2} = 2\pi m$

with m an integer, and at $E = 0, k = \pm\pi$ when $\frac{v}{2} - \frac{w}{2} = 2\pi m$ with m an integer. Remember that E and k are both periodic in 2π .

If the band gap closes at $E = \pm\pi$, we have $\lambda_{1,2}(k) = -1$, which gives

$$\begin{aligned} a_0 &= -1 \\ a_x^2 + a_y^2 &= 0 \end{aligned}$$

Similarly, we find that the bandgap closes at $E = \pm\pi, k = 0$ when $\frac{v}{2} + \frac{w}{2} = \pi + 2\pi m$, and at $E = \pm\pi, k = \pm\pi$ when $\frac{v}{2} - \frac{w}{2} = \pi + 2\pi m$ (m is an integer).

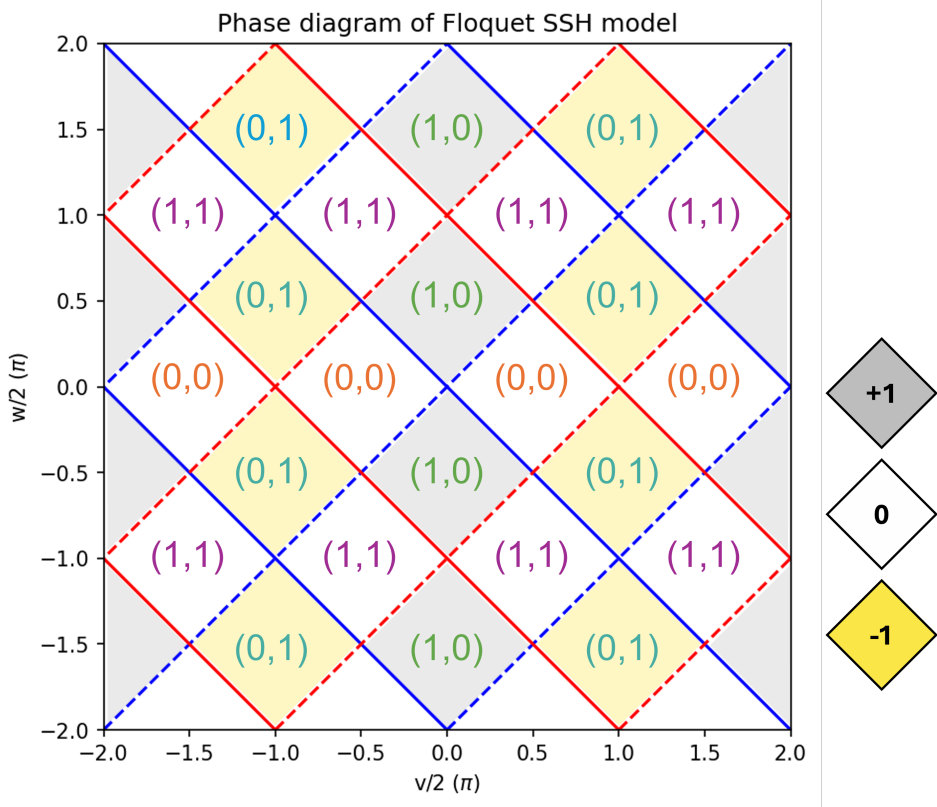


Figure 2.6: Phase diagram of the Floquet SSH lattice. On the solid blue lines the bandgap closes at $E = 0, k = 0$, on the dashed blue lines the bandgap closes at $E = 0, k = \pm\pi$, on the red solid lines the bandgap closes at $E = \pm\pi, k = 0$, on the red dashed lines the bandgap closes at $E = \pm\pi, k = \pm\pi$. The topological invariants (Q_0, Q_π) are calculated numerically in each region. The band topological invariant, which is not the true invariant, is calculated from the winding number of the effective Hamiltonian, and shown as different background color. See Ref [13] for a detailed description of the calculation.

The red and blue lines in Fig 2.6 shows when the phase can change due to closing of a

bandgap. The blue solid line corresponds to close at $E = 0, k = 0$, the blue dashed line corresponds to close at $E = 0, k = \pm\pi$, the red solid line corresponds to close at $E = \pm\pi, k = 0$, and the red dashed line corresponds to close at $E = \pm\pi, k = \pm\pi$.

Let's analyze the symmetry of the Hamiltonian.

The chiral symmetry is defined by

$$S^{-1}H(k, t)S = -H(k, -t)$$

where S is a unitary matrix. We can check that for our system

$$S = \sigma_z$$

During the period $0 \leq t < \frac{1}{4}$ and $\frac{3}{4} \leq t < 1$ when v is activated, we have

$$\begin{aligned} S^{-1}H(k, t)S &= \begin{pmatrix} 1 & 0 \\ 0 & -1 \end{pmatrix} \begin{pmatrix} 0 & v \\ v & 0 \end{pmatrix} \begin{pmatrix} 1 & 0 \\ 0 & -1 \end{pmatrix} \\ &= -\begin{pmatrix} 0 & v \\ v & 0 \end{pmatrix} = -H(k, -t) \end{aligned}$$

During the period $\frac{1}{4} \leq t < \frac{3}{4}$ when w is activated, we have

$$\begin{aligned} S^{-1}H(k, t)S &= \begin{pmatrix} 1 & 0 \\ 0 & -1 \end{pmatrix} \begin{pmatrix} 0 & we^{-ik} \\ we^{ik} & 0 \end{pmatrix} \begin{pmatrix} 1 & 0 \\ 0 & -1 \end{pmatrix} \\ &= -\begin{pmatrix} 0 & we^{-ik} \\ we^{ik} & 0 \end{pmatrix} = -H(k, -t) \end{aligned}$$

Notice that $H(k, t) = H(k, -t)$ due to our choice of the time origin.

A consequence of the chiral symmetry is that the eigenvalues of the full-period time evolution operator or the effective Hamiltonian are in pairs. If $|\psi_n\rangle$ is an eigenvector of $H_{\epsilon=0}^{\text{eff}}(k)$ with eigenvalue $E_n(k)$, then due to the chiral symmetry

$$\sigma_z H_{\epsilon}^{\text{eff}}(k) \sigma_z = -H_{-\epsilon}^{\text{eff}}(k) + \frac{2\pi}{T}$$

we have $H_{\epsilon=0}^{\text{eff}}(k)\sigma_z = -\sigma_z H_{\epsilon=0}^{\text{eff}}(k) + 2\pi\sigma_z$. Therefore,

$$\begin{aligned} H_{\epsilon=0}^{\text{eff}}(k)\sigma_z |\psi_n\rangle &= -\sigma_z H_{\epsilon=0}^{\text{eff}}(k) |\psi_n\rangle + 2\pi\sigma_z |\psi_n\rangle \\ &= (-E_n(k) + 2\pi)\sigma_z |\psi_n\rangle \end{aligned}$$

So $\sigma_z |\psi_n\rangle$ is also an eigenvector with eigenvalue $-E_n(k) + 2\pi$. Due to the periodicity of the quasienergy, the dispersion relation is symmetric around $E = q\pi$ in which q is an integer. As a result, the bandgap will only close at these quasienergy values.

For the particle-hole symmetry and the time-reversal symmetry, we check $C = \sigma_z$ and $T = I$, respectively, they should satisfy

$$\begin{aligned} C^{-1}H(k, t)C &= -H^*(-k, t) \\ T^{-1}H(k, t)T &= H^*(-k, -t) \end{aligned}$$

The topological invariants are affiliated with the gap quasienergy. It is defined as the winding number of the component of the periodized time evolution operator at $t = \frac{T}{2}$ (see Ref [13] for details). The periodized time evolution operator is

$$U_\epsilon(k, t) = U(k, t)e^{iH_\epsilon^{\text{eff}}(k)t}$$

where $H_\epsilon^{\text{eff}}(k)$ is the effective Hamiltonian, derived from the full-period time evolution operator $U(k, t = T)$. We also need to calculate the evolution operator at $t = \frac{1}{2}$, which is

$$\begin{aligned} U(k, t = \frac{1}{2}) &= e^{-i\frac{1}{4}(w\cos(k)\sigma_x + w\sin(k)\sigma_y)} e^{-i\frac{1}{4}\nu\sigma_x} \\ &= \left[\cos\left(\frac{\nu}{4}\right)\cos\left(\frac{w}{4}\right) - \sin\left(\frac{\nu}{4}\right)\sin\left(\frac{w}{4}\right)\cos(k) \right] I \\ &\quad - i \left[\sin\left(\frac{\nu}{4}\right)\cos\left(\frac{w}{4}\right) + \cos\left(\frac{\nu}{4}\right)\sin\left(\frac{w}{4}\right)\cos(k) \right] \sigma_x \\ &\quad - i \cos\left(\frac{\nu}{4}\right)\sin\left(\frac{w}{4}\right)\sin(k)\sigma_y \\ &\quad + i \sin\left(\frac{\nu}{4}\right)\sin\left(\frac{w}{4}\right)\sin(k)\sigma_z \end{aligned}$$

Finally, the invariants $\mathbb{Z} \times \mathbb{Z}$ are calculated numerically using the equation for AIII class (chiral class) after specifying ν, w in the phase diagram. To get the topological invariants, we can plot the $U_\epsilon^+(k)$ for different ν, w and count the number of its winding around the origin, which is shown in Fig 2.7.

We label each phase with its topological invariants given by the winding number (Q_0, Q_π) .

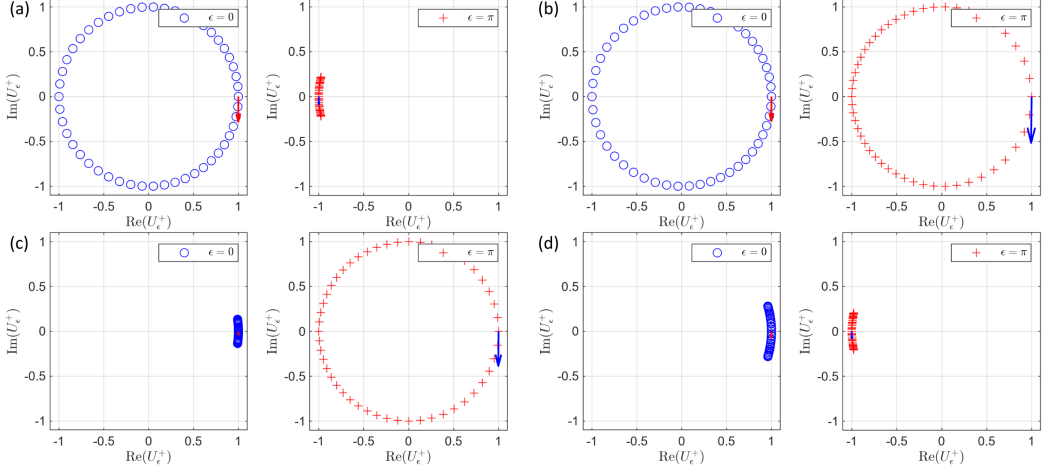


Figure 2.7: The winding number from the periodized time evolution operator for different ν, w , which gives the topological invariants of the Floquet SSH lattice. (a) $\nu = 0.2\pi, w = 1.2\pi$, (b) $\nu = 0.7\pi, w = 1.7\pi$, (c) $\nu = 1.8\pi, w = 0.9\pi$, (d) $\nu = 0.9\pi, w = 0.3\pi$. The arrows in the figures show the direction of the trajectory at $k = 0$ when k changing from 0 to 2π .

It's clear from the phase diagram that the closing of the bandgap leads to a change of the topological invariant affiliated with that gap. There are 4 phases in total.

3 Simulation

3.1 Code overview

The code used for simulating pulse evolution in the photonic mesh lattice can be found in Ref [15]. It enables an easy way to define the lattices to simulate, with settings of boundary condition, interface between lattices, input profile, and number of propagating steps. Moreover, it can be easily extended to simulate new types of lattices as long as the evolution equations (relations of input and output at a coupler) are known.

3.2 Evolution in a simple basic lattice

In Fig 3.1(a), the evolution of a single injected pulse in a simple basic lattice with 50/50 couplers is shown. As one can see from the dynamics in the long loop, the average position

of the pulse (particle) is moving away from the origin, showing a completely different feature from the classical random walk.

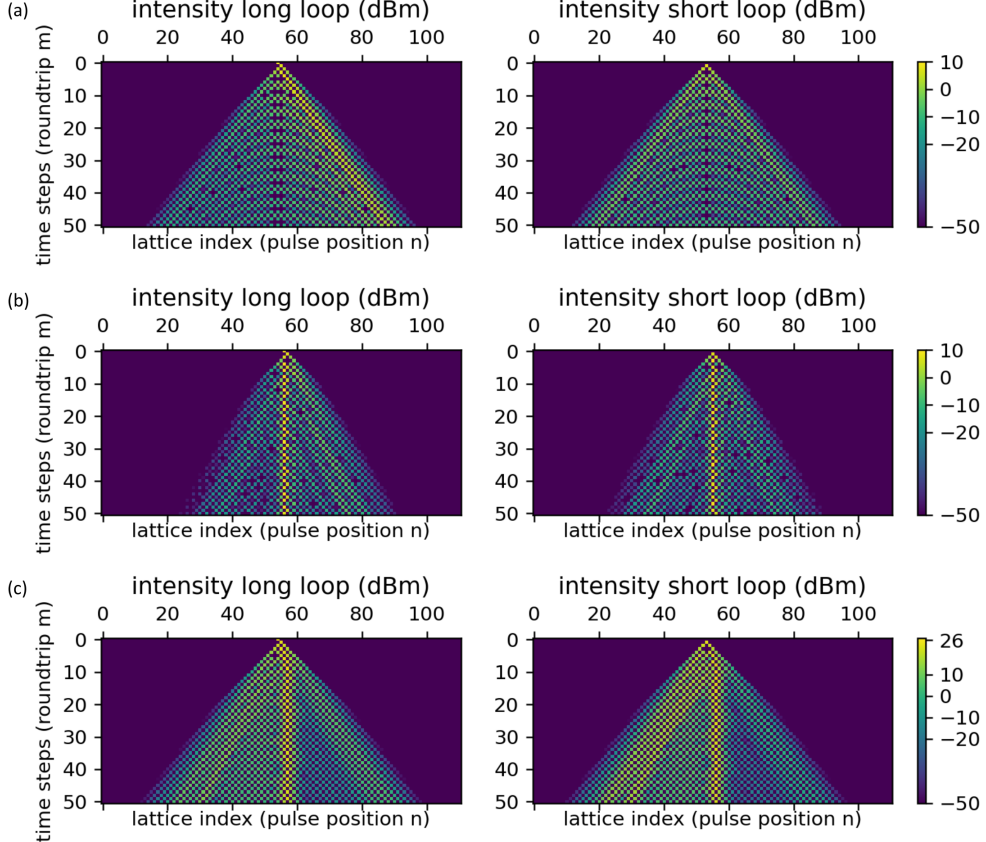


Figure 3.1: Evolution of a single injected pulse in different mesh lattices. The plot of the pulse intensity is in log scale. (a) A simple basic lattice with 50/50 couplers. (b) The Floquet SSH lattice with $\beta_o = 0.25\pi$, $\beta_e = 0.35\pi$ and $\beta_o = -0.75\pi$, $\beta_e = -0.65\pi$ separated by an interface. The two lattices have different gap invariants in both gaps but the same Floquet operator. (c) The 50/50 coupler lattice with nonlinear on-site potential from the self-phase modulation in 4 km loop of standard single mode fiber.

3.3 Evolution in the SSH lattice

The evolution in two SSH lattices separated by an interface is shown in Fig 3.1(b). The two lattices have different invariants $(0, 0)$ and $(1, 1)$ according to the phase diagram (Fig 2.6). Therefore, there should be two boundary states from the 0 gap and π gap, respectively. This can be seen from the simulation. An interesting thing is that these two lattices have the

same evolution operator (Floquet operator) based on the calculation in Appendix B. This demonstrates that the band topological invariant will fail in predicting the existence of boundary states in a Floquet system.

3.4 Evolution in a nonlinear lattice

The evolution in a 50/50 coupler lattice with nonlinear on-site potential is shown in Fig 3.1(c). The nonlinear on-site potential is achieved by exploiting self-phase modulation of the pulse in optical fiber[8]. In the simulation a 4 km long standard single mode fiber in each loop is considered, and the optical power required to have soliton state is ~ 500 mW. This power can be significantly reduced by replacing the fiber with high nonlinearity ones, such as dispersion compensating fiber. As shown in Fig 3.1(c), when we excite the lattice with a single pulse, it forms a localized, soliton-like state in the bulk and loses some of its energy as dispersive waves.

4 Experiment

4.1 Typical setup in papers

A typical experimental setup of coupled optical fiber loops is shown in Figure 4.1. The setup can be separated into three parts: pulse injection, loops, and signal detection. For the pulse injection, a continuous-wave laser is chopped into a single square pulse with a typical width of 10~100 ns and peak power of 0.1~1 mW. The large pulse width ensures negligible pulse broadening during the propagation, and a higher peak power with highly nonlinear fiber in the loops should be used if the nonlinear regime is exploited. The MZM and AOM are used together to have a higher suppression of the background, which turns out to be critical and limits the measurable roundtrips in my own setup.

For the loops, two spools of single mode fiber of different length are used for the two loops. The length difference in the two loops introduce a time delay between the pulses entering into the two loops. An optical coupler, here VBS, is used to join the two loops. The VBS can introduce a boundary between two bulk lattice with different phases. The EDFA are used to compensate for the losses during propagation, and BPF are used to reduce amplified spontaneous emission (ASE) noise and suppress lasing in the loops at the wavelength of peak emission probability of Erbium in optical fiber, which is around 1530 nm for my own

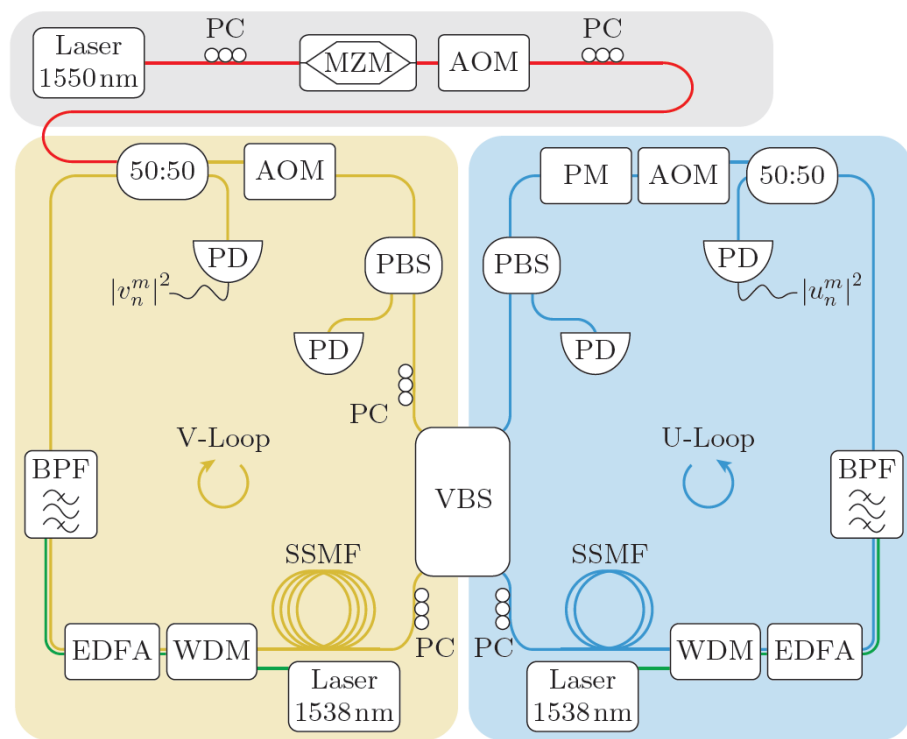


Figure 4.1: Experimental setup of coupled optical fiber loops in Ref [14]. MZM: Mach-Zehnder intensity modulator, AOM: acousto-optical intensity modulator, VBS: variable beam splitter, PD: photodetectors, SSMF: standard single mode fiber, WDM: wavelength-division multiplexing coupler, BPF: bandpass filters, PM: phase modulator, PBS: polarization beam splitter, PC: polarization controllers.

setup. To reduce the gain oscillation of EDFA when amplifying the pulse train, a continuous-wave pilot laser at 1538 nm different from the signal wavelength is used to clamp the gain of EDFA to suppress its transient response, and is also filtered out by the BPF. The AOMs in the loops are used to implement switchable gain/loss for non-Hermitian applications, and can also be used to suppress the background where there is no signal pulse. PM is used to introduce a tunable on-site potential for the lattice, and together with AOM, they can generate an excitation pulse train with Gaussian distribution[16], which is useful for probing a narrow bandwidth in the reciprocal space. PC are used to adjust polarization before polarization-sensitive devices and to ensure interference.

The pulses that can interfere need to have the same number of roundtrips both in the long loop and the short loop, which makes the setup robust to slow fluctuations that will change the accumulated phase. A detailed discussion is in the Appendix A.

For the signal detection, an optical coupler in each loop is used. And the loss caused by detection is also compensated by EDFA in the loops. The typical pulse width is \sim 50 ns and distance between neighboring pulses is \sim 100 ns. Therefore a detector with 1 GHz bandwidth will be very sufficient. The electrical signal will be recorded by a digital storage oscilloscope. A low-noise, high-responsivity detector is preferred since the peak power of the pulses is usually decreasing after each roundtrips.

4.2 Current setup

To investigate the performance of the coupled optical fiber loops, a setup is built in the PHOSL lab at EPFL with least required components. As shown in Figure 4.2, a tunable continuous-wave laser outputs at 1550 nm with maximum power of 4 mW. The light is amplified to 10 mW by EDFA and then modulated into a pulse train. The pulses are square-shaped and have a width of 70 ns and repetition rate of \sim 1 kHz. The use of pulse train is to repeat the measurement after the previous pulses have sufficiently decayed in the loops. The pulse injected into the long loop has a peak power of \sim 1 mW, owing to losses in the devices and fiber adapters. A 50/50 coupler is used to join the two loops, where each one includes \sim 2 km spool of fiber. A home built EDFA in each loop compensates the roundtrip losses. The 980 nm pump is coupled into the loop through WDM and \sim 55 cm Erbium-doped fiber is used to amplify the signal. An isolator is used to eliminate backscattering and a BPF is used to suppress lasing, reduce ASE and filter out the pump. Only the pulses in the long loop are detected, using the same coupler for pulse injection.

The performance of the current setup is limited by the noise from the background of

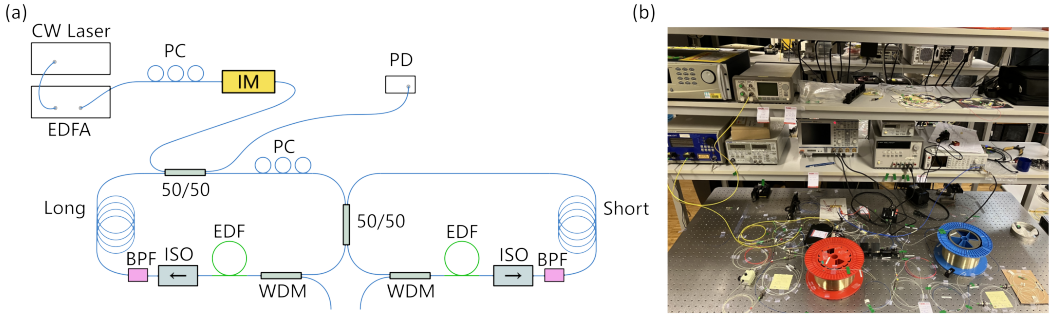


Figure 4.2: The current experimental setup built in PHOSL. (a) Schematic of the setup. EDF: Erbium doped fiber; IM: intensity modulator. (b) The photo of the real setup.

the pulse train. This background comes from the finite extinction ratio of the intensity modulator in the pulse injection path. When the modulator is turned “off”, there will still be a small amount of light continuously passing through and coupled into the loops, which is then amplified and interferes with time-delayed background. This happens over and over again, leading to a large and fluctuating background at the detector that floods the pulse signal. This can be improved, as is done in many papers, by adding another intensity modulator in series in the pulse injection path, or adding an intensity modulator in each loop that is synchronized to the pulse roundtrip to suppress the background during each roundtrip.

The measurement is done in the following steps: first, one pulse is injected into the loops with no gain in the EDF. The pulse amplitude will decay to zero before completing one roundtrip. Then, we gradually increase the power of the pump laser in each loop and monitor the pulse train after the second roundtrip, which contains two pulses separated by the time delay corresponding to the length difference between two loops. By making the amplitude of two pulses equal, one can control the two loops to have the same net gain/loss. Then we monitor the pulse train after the fifth roundtrip, which contains five pulses. However, if the polarization is aligned, which means the polarization change after one roundtrip in each loop is the same, the second and third position in the pulse train will have destructive interference and no light will be seen. Therefore, we can align the polarization controller after this step and start recording the result. Due to the large background fluctuation, we should take an average of multiple measurements. This is done by generating a ~ 1 kHz pulse train in the injection path and perform an average using the built-in function in the oscilloscope. The net gain/loss is **not** precisely controlled, for example, to be exactly zero net gain. To do this, we may compare the ratio of pulse amplitude between different roundtrips with the simulation.

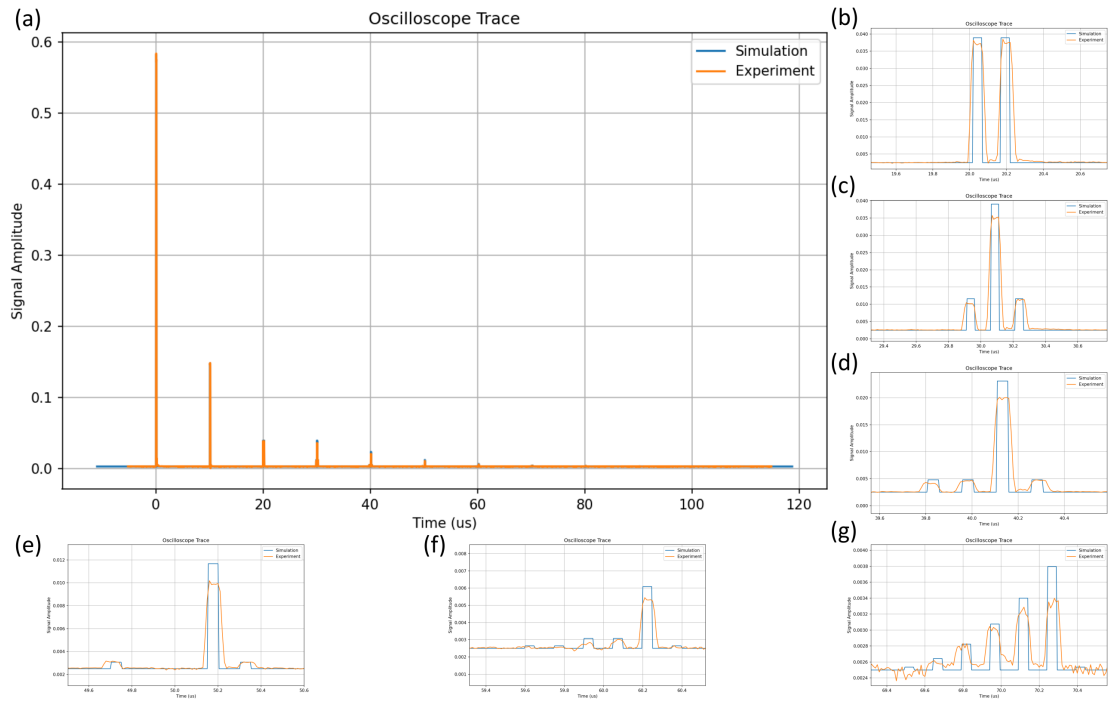


Figure 4.3: Experimental result from the current setup, compared with simulation. Parameters chosen for simulation: 50/50 coupler, 3dB loss in each loop, 50 ns pulse width (70 ns in experiment from AWG), 9.97 us roundtrip time, 150 ns time difference in two loops. The fitting of simulation to the experimental result is done by adjusting the parameters manually. (b)-(g) are the zoomed view of the trace in (a).

The pulse train circulating in the long loop is measured and the trace in an oscilloscope is shown in Fig 4.3. The fifth roundtrip and destructive interference is clearly seen from Fig 4.3(e). However, the maximum observable roundtrip is very limited compared to more than 100 in many papers. The main reason is considered to be the continuous background of the injected pulse train, which is also amplified and interferes with the pulses. In addition, this background will compete with the pulses for the gain of EDF, hindering further compensating the losses even if increasing the pump power. The degradation from the background can be mitigated by adding another intensity modulator in the injection path to have a higher extinction ratio, or using intensity modulators in the loops as a time gate to selectively suppress the background. Note that the measurement result comes from averaging multiple traces, where a new 0th roundtrip pulse is injected after the previous pulse train is sufficiently decayed into the background. If we didn't take the average, the traces would be fluctuating violently due to the amplified background.

4.3 Future work

To improve the experimental setup, the background fluctuation should be suppressed, and the methods are discussed in the previous paragraphs. To have more flexibility, and play with Floquet system or add disorders, we can add phase modulators in the loops and replace the 50/50 coupler by a variable coupler. The phase modulator can also be used to extend the reachable region in the phase diagram, which is discussed in the Appendix. Instead of a variable coupler, an optical on/off switch can also be used for faster modulation speed. Besides, the interplay of nonlinearity and topology is also a topic of interest. Usually a spool of dispersion compensating fiber is used for a higher nonlinear coefficient, which introduces a nonlinear on-site potential to the synthetic lattice. However, it is challengeable to have a nonlinear coupling between the sites, which can lead to self-induced topological phase transition[17].

As a playground to implement many exotic theoretical models, one may ask if the coupled optical fiber loops can have some applications, for example, complex light manipulation, which has been explored recently[18]. The setup may offer a solution for waveform generation, single-shot pulse autocorrelation, and optical neural network.

5 Conclusion

This project explores the basics of the coupled optical fiber loops for synthetic photonic mesh lattices and topological photonics. The band structure and topological invariants of some typical lattices are calculated, which can be generalized to other lattices. A script for simulating pulse evolution in mesh lattices is provided. It is able to deal with interfaces and boundaries, and can be easily extended to simulate new lattices. A very basic experimental setup is built, which successfully demonstrates a few steps of propagation. Future work should try to improve the performance of the setup and add more functionalities, such as intensity, phase modulation and variable coupling ratio.

6 Acknowledgements

Junda Wang and Zhe Zhang guided me into the world of topological insulators and topological photonics. Ji Zhou helped me a lot on building the setup. Jiaye Wu assisted me using the fiber winding machine and OTDR. Professor Camille Brès provided valuable advice for building the setup. Professor Romain Fleury supervised the project. The setup is built in the photonic systems laboratory (PHOSL) at EPFL.

References

1. Regensburger, A., Bersch, C., Hinrichs, B., Onishchukov, G., Schreiber, A., Silberhorn, C. & Peschel, U. Photon propagation in a discrete fiber network: an interplay of coherence and losses. *Physical Review Letters* **107**, 233902. <https://link.aps.org/doi/10.1103/PhysRevLett.107.233902> (2011).
2. Miri, M.-A., Regensburger, A., Peschel, U. & Christodoulides, D. N. Optical mesh lattices with PT symmetry. *Physical Review A* **86**, 023807. <https://link.aps.org/doi/10.1103/PhysRevA.86.023807> (2012).
3. Regensburger, A., Bersch, C., Miri, M.-A., Onishchukov, G., Christodoulides, D. N. & Peschel, U. Parity-time synthetic photonic lattices. *Nature* **488**, 167–171. <https://www.nature.com/articles/nature11298/> (2012).
4. Wimmer, M., Regensburger, A., Miri, M.-A., Bersch, C., Christodoulides, D. N. & Peschel, U. Observation of optical solitons in PT-symmetric lattices. *Nature Communications* **6**, 7782. <https://www.nature.com/articles/ncomms8782> (2015).
5. Weidemann, S., Kremer, M., Helbig, T., Hofmann, T., Stegmaier, A., Greiter, M., Thomale, R. & Szameit, A. Topological funneling of light. *Science* **368**, 311–314. <https://www.science.org/doi/10.1126/science.aaz8727> (2020).
6. Weidemann, S., Kremer, M., Longhi, S. & Szameit, A. Topological triple phase transition in non-hermitian floquet quasicrystals. *Nature* **601**, 354–359. <https://www.nature.com/articles/s41586-021-04253-0> (2022).
7. Yu, L., Xue, H., Guo, R., Chan, E. A., Terh, Y. Y., Soci, C., Zhang, B. & Chong, Y. D. Dirac mass induced by optical gain and loss. *Nature* **632**, 63–68. <https://www.nature.com/articles/s41586-024-07664-x> (2024).
8. Bisianov, A., Wimmer, M., Peschel, U. & Egorov, O. A. Stability of topologically protected edge states in nonlinear fiber loops. *Physical Review A* **100**, 063830. <https://link.aps.org/doi/10.1103/PhysRevA.100.063830> (2019).
9. Feis, J., Weidemann, S., Sheppard, T., Price, H. M. & Szameit, A. *Spacetime-topological events* 2024. arXiv: 2407.02176. <https://arxiv.org/abs/2407.02176>.
10. Ren, Y., Ye, K., Chen, Q., Chen, F., Zhang, L., Pan, Y., Li, W., Li, X., Zhang, L., Chen, H. & Yang, Y. Observation of momentum-gap topology of light at temporal interfaces in a time-synthetic lattice. *Nature Communications* **16**, 707. <https://www.nature.com/articles/s41467-025-56021-7> (2025).
11. Wimmer, M. *Experiments on photonic mesh lattices* PhD thesis (2018). <https://open.fau.de/handle/openfau/10213>.

12. Kitagawa, T., Broome, M. A., Fedrizzi, A., Rudner, M. S., Berg, E., Kassal, I., Aspuru-Guzik, A., Demler, E. & White, A. G. Observation of topologically protected bound states in photonic quantum walks. *Nature Communications* **3**, 882. <https://www.nature.com/articles/ncomms1872> (2012).
13. Yao, S., Yan, Z. & Wang, Z. Topological invariants of Floquet systems: General formulation, special properties, and Floquet topological defects. *Physical Review B* **96**, 195303. <https://link.aps.org/doi/10.1103/PhysRevB.96.195303> (2017).
14. Weidemann, S. *Non-hermitian topological photonics in coupled optical fibre loops* Dissertation (Universität Rostock, 2022). https://rosdok.uni-rostock.de/resolve/id/rosdok_disshab_0000002955.
15. See GitHub repository https://github.com/nlphotronics/light_walk_in_two_loops.
16. Wimmer, M., Regensburger, A., Bersch, C., Miri, M.-A., Batz, S., Onishchukov, G., Christodoulides, D. N. & Peschel, U. Optical diametric drive acceleration through action-reaction symmetry breaking. *Nature Physics* **9**, 780–784. <https://www.nature.com/articles/nphys2777> (2013).
17. Hadad, Y., Khanikaev, A. B. & Alù, A. Self-induced topological transitions and edge states supported by nonlinear staggered potentials. *Physical Review B* **93**, 155112. <https://link.aps.org/doi/10.1103/PhysRevB.93.155112> (2016).
18. Monika, M., Nosrati, F., George, A., Sciara, S., Fazili, R., Marques Muniz, A. L., Bisianov, A., Lo Franco, R., Munro, W. J., Chemnitz, M., Peschel, U. & Morandotti, R. Quantum state processing through controllable synthetic temporal photonic lattices. *Nature Photonics* **19**, 95–100. <https://www.nature.com/articles/s41566-024-01546-4> (2025).
19. Kitagawa, T. Topological phenomena in quantum walks: elementary introduction to the physics of topological phases. *Quantum Information Processing* **11**, 1107–1148. <https://doi.org/10.1007/s11128-012-0425-4> (2012).

Appendix A: Influence of phase ambiguity in the coupler and loops

When propagating in either the long loop or the short loop, the pulse will acquire an arbitrary phase shift. The origin of this phase includes the photoelastic effect from the randomly distributed strain over the fiber loop, and thermorefractive effect due to temperature drift in the environment. The good thing is that this phase, although unable to determine, can be assumed constant because the time scale of a large part of fluctuations is much slower than one measurement is performed (<1 ms). And the high frequency fluctuations can be further reduced by better vibration isolation and temperature control.

We can then define the unknown but constant phase shift as $\varphi_{\text{long loop}}$, $\varphi_{\text{short loop}}$, as shown in the left side of Figure A.1. Now we will show that this phase shift has no effect to the interferometric experiment result. Because they are constant and only the pulses traveling the same times in two loops can interfere, all the pulses will have the same phase shift $\varphi_{\text{long loop}}^p \varphi_{\text{short loop}}^q$, where p, q are roundtrips in long and short loop. This overall phase will be cancelled out and have no influence in the interference.

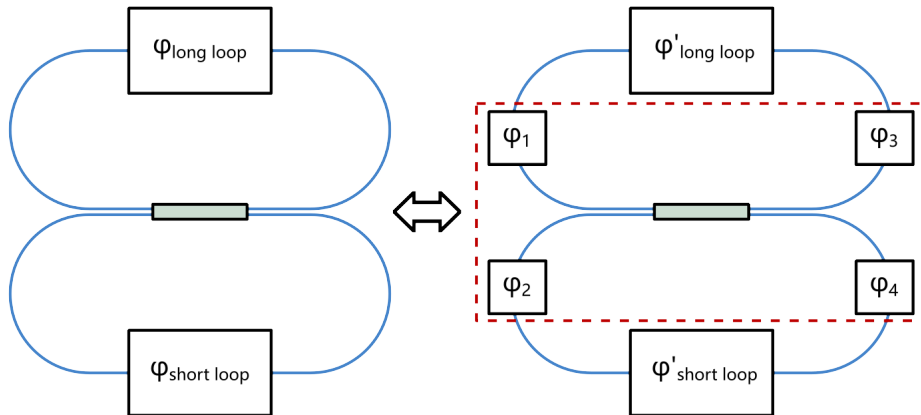


Figure A.1: The freedom of defining the phase shift in the four ports of the coupler between the two loops. The unknown but constant phase shift in the two loops can be spared to the coupler, $\varphi_{\text{long loop}} = \varphi'_{\text{long loop}} + \varphi_1 + \varphi_3$ (similar for the short loop), which leads to an effectively new coupler with a different transfer matrix.

However, we should emphasize that the change of polarization state of light in the two loops must be compensated to the same value, which is not required for the phase shift as discussed above. This is because the polarization state is not a scalar value but can be represented by a vector on the Poincaré sphere. The change of polarization state, which is a

rotation operation on the sphere, does not commute. This is also why the pulse train will change its distribution when we rotate the polarization controller in the loop.

Another issue is the ambiguity in the transfer matrix of the coupler between the two loops. For a 50/50 coupler we have chosen a symmetric matrix throughout the discussion

$$\mathcal{M}_0 = \frac{1}{\sqrt{2}} \begin{pmatrix} 1 & i \\ i & 1 \end{pmatrix} \quad (1)$$

However, in a real experiment we may find 50/50 couplers with different transfer matrix, for example,

$$\mathcal{M}_1 = \frac{1}{\sqrt{2}} \begin{pmatrix} 1 & 1 \\ 1 & -1 \end{pmatrix} \quad (2)$$

is also often used. Moreover, in practice the two output ports of a 50/50 coupler may be interchanged, which leads to

$$\mathcal{M}_2 = \frac{1}{\sqrt{2}} \begin{pmatrix} i & 1 \\ 1 & i \end{pmatrix} \quad (3)$$

or

$$\mathcal{M}_3 = \frac{1}{\sqrt{2}} \begin{pmatrix} 1 & -1 \\ 1 & 1 \end{pmatrix} \quad (4)$$

One may ask if this phase ambiguity in the coupler will change the dynamics of light propagation. We will show that these transfer matrices all lead to the same dynamics. The phase shift in each loop can be separated into three parts as in Figure A.1. This means we have the freedom to choose an arbitrary phase in all the four ports of the coupler, without changing the experimental result. This means all the transfer matrices having the form

$$\frac{1}{\sqrt{2}} \begin{pmatrix} e^{i\varphi_3} & 0 \\ 0 & e^{i\varphi_4} \end{pmatrix} \begin{pmatrix} 1 & i \\ i & 1 \end{pmatrix} \begin{pmatrix} e^{i\varphi_1} & 0 \\ 0 & e^{i\varphi_2} \end{pmatrix} \quad (5)$$

will have the same result as \mathcal{M}_0 . One can verify that we can get \mathcal{M}_1 when we choose $\varphi_1 = -\frac{\pi}{2}$, $\varphi_2 = \pi$, $\varphi_3 = \frac{\pi}{2}$, $\varphi_4 = 0$, \mathcal{M}_2 when we choose $\varphi_1 = -\frac{\pi}{2}$, $\varphi_2 = \frac{\pi}{2}$, $\varphi_3 = \pi$, $\varphi_4 = 0$, \mathcal{M}_3 when we choose $\varphi_1 = -\frac{\pi}{2}$, $\varphi_2 = 0$, $\varphi_3 = \frac{\pi}{2}$, $\varphi_4 = 0$.

Appendix B: Quantum walk formulation of the Floquet SSH lattice

Here we try to analyze the Floquet SSH lattice in the framework of discrete-time quantum walk[19]. We first define some notations:

Spin :

$$a : |\uparrow\rangle = |0\rangle = \begin{pmatrix} 1 \\ 0 \end{pmatrix}$$

$$b : |\downarrow\rangle = |1\rangle = \begin{pmatrix} 0 \\ 1 \end{pmatrix}$$

Pauli matrices :

$$\sigma_x = \begin{pmatrix} 0 & 1 \\ 1 & 0 \end{pmatrix}$$

$$\sigma_y = \begin{pmatrix} 0 & -i \\ i & 0 \end{pmatrix}$$

$$\sigma_z = \begin{pmatrix} 1 & 0 \\ 0 & -1 \end{pmatrix}$$

$$I = \begin{pmatrix} 1 & 0 \\ 0 & 1 \end{pmatrix}$$

Rotation operator :

$$R(\beta) = e^{i\beta\sigma_x} = \begin{pmatrix} \cos(\beta) & i\sin(\beta) \\ i\sin(\beta) & \cos(\beta) \end{pmatrix}$$

The discrete-time quantum walk for a 2-spin particle is achieved by a rotation operator followed by a spin-dependent translation operator. For a finite, periodic lattice with N sites, the translation operator is defined as

$$T = \sum_{x=1}^N |x+1\rangle\langle x| \otimes |\uparrow\rangle\langle\uparrow| + |x-1\rangle\langle x| \otimes |\downarrow\rangle\langle\downarrow|$$

It can be verified that the evolution operator on the Floquet SSH lattice is

$$U = TR(\beta_e)TR(\beta_o)$$

Note that U is $N/2 \times N/2$ dimension instead of $N \times N$ because only the odd sites can be taken for the input state and states after applying U . By transforming the position basis to the momentum basis, the evolution operator can be written as

$$U = \sum_k |k\rangle\langle k| \otimes U_k, \text{ where } k = \frac{2\pi l}{N/2}, l = 1, 2, \dots, N/2$$

where $|k\rangle = \frac{1}{\sqrt{N/2}} \sum_{n=1}^{N/2} e^{ikn} |2n-1\rangle$ is the Fourier-transformed state and U_k is the 2×2 matrix acting on the spin state:

$$U_k = \begin{pmatrix} \cos(\beta_e) \cos(\beta_o) e^{-ik} - \sin(\beta_e) \sin(\beta_o) & i \cos(\beta_e) \sin(\beta_o) e^{-ik} + i \sin(\beta_e) \cos(\beta_o) \\ i \cos(\beta_e) \sin(\beta_o) e^{ik} + i \sin(\beta_e) \cos(\beta_o) & \cos(\beta_e) \cos(\beta_o) e^{ik} - \sin(\beta_e) \sin(\beta_o) \end{pmatrix}$$

The Floquet theorem states that:

$$U_k |\psi_{k,E}\rangle = e^{-iE} |\psi_{k,E}\rangle$$

This is equivalent to the ABCD matrix that we have derived before. The k, E here correspond to $Q, -\theta$. The dispersion relation can be obtained in the same way.

$$\cos(E) = \cos(\beta_e) \cos(\beta_o) \cos(k) - \sin(\beta_e) \sin(\beta_o)$$

The evolution operator is characterized by a rotation around an axis in the Bloch sphere and can be decomposed into the superposition of the Pauli matrices:

$$U_k = R_n(\alpha) = e^{-i\frac{\alpha}{2}\vec{n}\cdot\vec{\sigma}} = \cos\left(\frac{\alpha}{2}\right)I - i \sin\left(\frac{\alpha}{2}\right)\vec{n}\cdot\vec{\sigma}$$

$$\cos\left(\frac{\alpha}{2}\right) = \cos(\beta_e) \cos(\beta_o) \cos(k) - \sin(\beta_e) \sin(\beta_o) = \cos(E)$$

$$\vec{n} = \frac{1}{\sin(E)} \begin{pmatrix} -\sin(\beta_o) \cos(\beta_e) \cos(k) - \cos(\beta_o) \sin(\beta_e) \\ -\sin(\beta_o) \cos(\beta_e) \sin(k) \\ \cos(\beta_o) \cos(\beta_e) \sin(k) \end{pmatrix}$$

There is a vector that is perpendicular to all the \vec{n} for different k :

$$\vec{A} = \begin{pmatrix} 0 \\ \cos(\beta_o) \\ \sin(\beta_o) \end{pmatrix}$$

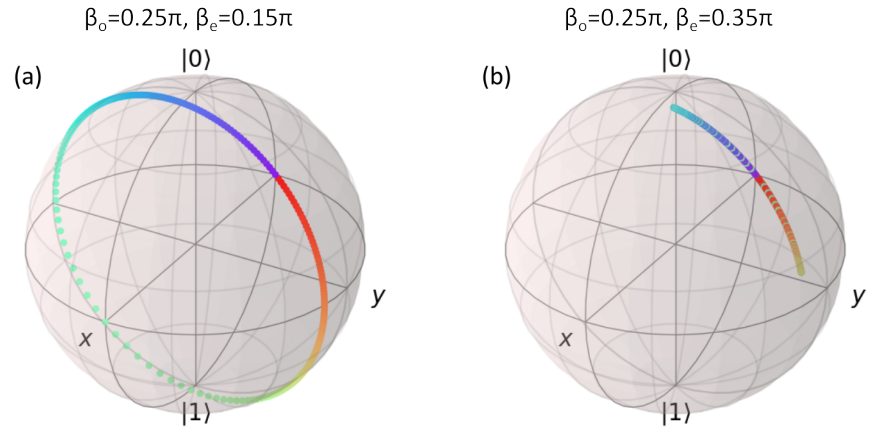


Figure B.1: The Bloch sphere showing the winding number of \vec{n} calculated from the evolution operator. The color of dots represents \vec{n} for different k from 0 to 2π .

The winding number is obtained by counting the times that \vec{n} winds around the Bloch sphere when k goes from 0 to 2π , which is shown in Fig B.1. The \vec{n} will always go back to its starting point because it is periodic in 2π .

Appendix C: Extending the experimentally reachable region in the phase diagram

The phase diagram of the Floquet SSH lattice shown in Fig 2.6 leads to an experimental difficulty. As β_o, β_e can only take values between 0 and $\pi/2$, corresponding to a 100/0 or 0/100 coupler, the region in phase space that we can immediately get is $v/2, w/2 \in [0, \pi/2]$. Therefore, we can only achieve two phases out of four in experiment.

This can be solved using phase modulators, one in each loop, to effectively have more values of β_o, β_e . The transfer matrix of an optical coupler can be expressed as

$$\begin{pmatrix} \cos(\beta) & i \sin(\beta) \\ i \sin(\beta) & \cos(\beta) \end{pmatrix}$$

If we have phase modulation in one loop before and after the coupler

$$\begin{pmatrix} -1 & 0 \\ 0 & 1 \end{pmatrix} \begin{pmatrix} \cos(\beta) & i \sin(\beta) \\ i \sin(\beta) & \cos(\beta) \end{pmatrix} \begin{pmatrix} -1 & 0 \\ 0 & 1 \end{pmatrix} = \begin{pmatrix} \cos(\beta) & -i \sin(\beta) \\ -i \sin(\beta) & \cos(\beta) \end{pmatrix} = \begin{pmatrix} \cos(-\beta) & i \sin(-\beta) \\ i \sin(-\beta) & \cos(-\beta) \end{pmatrix}$$

We can map β to $-\beta$. We also note that the order of the three operation (phase modulation, optical coupler, phase modulation) can change by shifting the time origin, therefore we only need one modulator which adds a 2π phase shift.

Now think of another scenario, if we have phase modulation in each loop, we can get

$$\begin{pmatrix} -1 & 0 \\ 0 & -1 \end{pmatrix} \begin{pmatrix} \cos(\beta) & i \sin(\beta) \\ i \sin(\beta) & \cos(\beta) \end{pmatrix} = \begin{pmatrix} -\cos(\beta) & -i \sin(\beta) \\ -i \sin(\beta) & -\cos(\beta) \end{pmatrix} = \begin{pmatrix} \cos(\pi + \beta) & i \sin(\pi + \beta) \\ i \sin(\pi + \beta) & \cos(\pi + \beta) \end{pmatrix}$$

Therefore, we can map β to $\pi + \beta$. Combining the two modulation, we can get any β in $[-\pi/2, 3\pi/2]$ starting from a value in $[0, \pi/2]$. The extended region has a length of 2π , which covers one period in the phase diagram. So we effectively reach all the four phases.